Analysis of Shockwave Radiation Data in Nitrogen

Brett A. Cruden[1], Aaron M. Brandis[2]
AMA, Inc. at NASA Ames Research Center, Moffett Field, CA, 94035

Data from test series in the Electric Arc Shock Tube Facility were previously reported for velocities spanning 6-12 km/s in pure N_2 at a freestream pressure of 0.2 Torr. The test series provided spectrally- and spatially-resolved data for validation of a number of models of physical phenomena, including vibrational relaxation, molecular radiation, nitrogen dissociation and ionization, and atomic radiation and ionization. In the present work analysis of data obtained at a nominal velocity of 10.3 km/s is discussed in detail. Spectra are analyzed to extract temperatures and the densities of excited states as a function of position behind the shock. The effect of different methods for calculating state populations and ionization processes is assessed, as is a rigorous assessment of the atomic line lists, with both missing and extra lines identified.

I.   Introduction

Over the last decade, NASA has conducted a number of shock tube test campaigns to better quantify radiative heating from the bow shock around vehicles entering the Earth's atmosphere at hyperbolic velocities. These tests have therefore focused on N_2 and O_2 mixtures. Although these measurements have generally shown very good agreement (~17%) with predictions for equilibrium radiation [1], the non-equilibrium contribution is less well predicted (~50%) [2]. In terms of surface heating, these, and other factors, led to overall uncertainties of 42% for radiative heating in Lunar-return entries [3]. With a view toward reduction of uncertainties in nonequilibrium radiation predictions, modifications were made to molecular models and the improvements were demonstrated by comparing to tests performed at 7-9 km/s [4]. While these improvements were made with a small number of adjustable parameters, it is desirable to remove confounding effects created by the complexity of the mixture under study by examining a simpler system such as molecular nitrogen. At the same time, there has been a significant amount of theoretical work on molecular nitrogen using *ab initio* methods such as DMS and QCT [5-8]. These works have shown good agreement with current practices in nitrogen dissociation rates, but have cast doubts on modelling parameters such as vibrational relaxation times, Boltzmann modelling of vibrational states, and the influence of atomic collision partners on dissociation rates. For these reasons, a study of nitrogen chemistry was conducted in the Electric Arc Shock Tube (EAST) facility at NASA Ames [9]. This study measured radiation as a function of position behind the shock from deep vacuum ultraviolet through near-infrared spectral ranges (120-1600 nm) and velocities from 6 to 12 km/s at a constant freestream pressure (0.2 Torr). The study thus included a wide range of physical phenomena, including vibrational relaxation, molecular dissociation, and atomic/molecular ionization. Features observed in the test include radiation from atomic lines of N, 1st and 2nd Positive bands of N_2, and the 1st Negative band of N_2^+. Ionization was calculated by measuring a hydrogen contaminant line at high resolution and obtaining electron density data through determining the Stark broadening component.

In the work of Brandis and Cruden [9], 17 shots were identified as "benchmark" cases for further study. A composite spectrum in the non-equilibrium region from two such cases with similar velocity is shown in Figure 1 with major spectral features identified.

[1] Sr. Research Scientist, Aerothermodynamics Branch. Associate Fellow AIAA. Contact: brett.a.cruden@nasa.gov
[2] Sr. Research Scientist, Aerothermodynamics Branch. Associate Fellow AIAA.
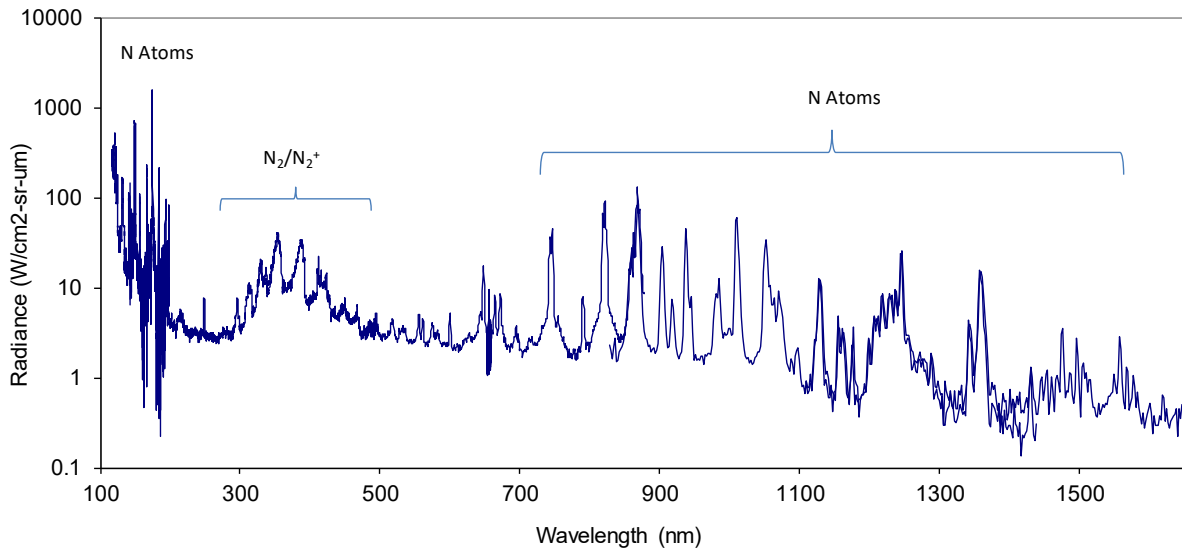
Figure 1. Composite spectrum of non-equilibrium radiance for nitrogen shocked at 10.32-10.34 km/s

This paper focuses on the 10.34 and 10.32 km/s conditions specifically, performing analysis of the spectral data to obtain trends in excited species densities and temperatures as a function of position behind the shock.

II. Approach
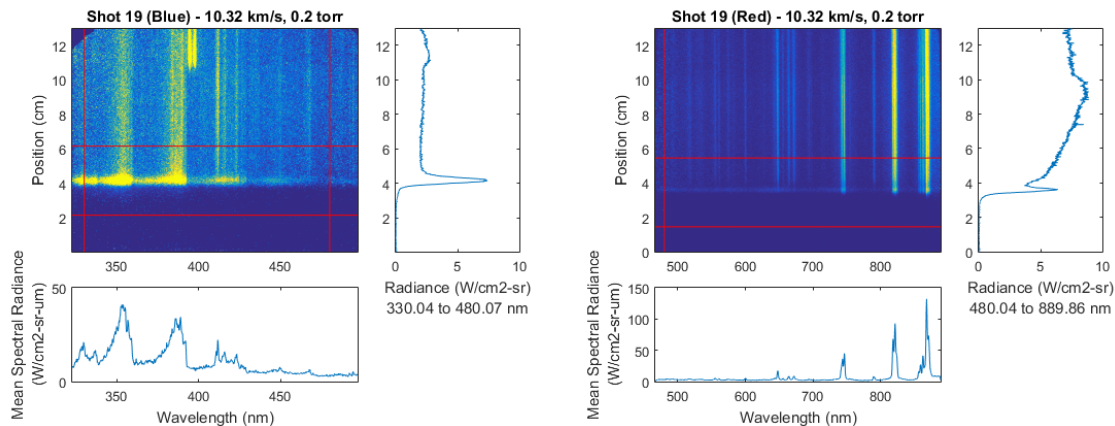
Figure 2. 3D spectral intensity maps obtained at 10.3 km/s in the ultraviolet and visible regions

An example of the data obtained from these tests is shown in Figure 2. The data are spectrally and spatially resolved, giving a 3D map of radiance versus these two variables. Horizontal slices through the image yield spectra such as that presented in Figure 1 which can be used for verification of radiation models or, as in this work, to obtain information about radiating species through analysis. Spatial resolution along the y-axis may be used to interpret the data as a function of position and study phenomena such as relaxation or reaction rates [4, 10, 11]. The position in Figure 2 represents the axial position on the observation window. Regions behind the initial transient are referred to here as the "steady" region and in the past has been thought to represent the equilibrium region of the shock. For purposes of analysis, the mean spectrum between 1 and 6 cm behind the shock front is analyzed and compared to equilibrium predictions. In previous works [2, 4, 12, 13], the spatial trend has been analyzed in terms of integrated spectral radiance over certain bandwidths, which may be used as a check on the integrated spectrum or the contribution from a particular line or species. In this work, the spectra themselves are analyzed to obtain spatially resolved data. Each camera has 1024 pixel rows, with each pixel representing about 0.013 cm along the tube axis. In order to obtain sufficient signal to noise, 20 pixel rows have been binned for each spectrum. In addition to the binning, the spatial resolution of the data is limited by the motion of the shock during camera gating and by charge spread across rows on the charge coupled device (CCD). Except in the last section, the impact of this spatial

resolution is not considered in presenting data extracted through spectral fitting, and the data are presented as discrete points along the spatial dimension. An additional consideration in presenting the spatial data is the location of the shock front. Shock arrival in the EAST is determined by PCB brand piezoelectric pressure transducers. The initial inflection in the pressure trace is used to set the arrival time at the location of the transducer, and these data are used to construct a fit of shock arrival versus time (i.e. x-t fit) [14]. Since the trigger time of the cameras is known, the x-t relationship sets the position of the shock at the time the image is taken. The spatial dimension can thus be translated to put the y-axis at the location of the shock. The accuracy of this approach is determined by the accuracy of the x-t fit and the accuracy of alignment of the optics relative to transducer placement. We estimate the latter as dominating the uncertainty in shock position at approximately 3 mm. There may be an additional 1-2 mm of uncertainty attributable to factors that enter the x-t fit, such as the spatial extent and temporal lag time of the pressure sensor.

Spectra from these shots are analyzed to obtain number densities of electronic states responsible for radiation as a function of position behind the shock. A code was written to obtain best fit spectra through repeated calls to NEQAIR[15, 16] with varying input parameters. This code is built upon the Python *numpy* library and includes a user interface for calling NEQAIR and performing optimizations based upon PyQT. This interface will be packaged with a future version of NEQAIR. NEQAIR constructs spectral radiance profiles given an input of temperatures and species number densities; here treating each shock tube location as a line with constant properties (i.e. a 1-D flow). The first step in obtaining a radiation solution is to determine the distribution of excited states. NEQAIR may generate the state distribution by assuming a Boltzmann relationship, or may solve a reaction kinetic equation for the electronic levels to obtain a non-Boltzmann solution. A third alternative is to read in the state population from a file, which is here generated as part of the fitting process. Once the state populations are known, the radiance may be calculated using dipole moments or Einstein coefficients. The Einstein coefficients for atomic lines, which figure prominently in this work, originate from the NIST atomic spectral database [17]. Molecular dipole moments come from various sources, depending on the band system.

Initial fits were performed in the steady region of the shot using the non-Boltzmann option of NEQAIR. This involved a simultaneous fit of temperatures ($T_t=T_r$ and $T_v=T_e=T_{e^-}$)* and the species N, N_2, N_2^+ and N^+, with e^- density determined by quasi-neutrality. For some cases, it was found useful to add impurities in the spectra, such as C, H and CN. The fit solutions obtained are not necessarily unique. For example, a feature dependent upon the density of a particular excited state could be replicated by a nearly continuous relationship of ground state density and electronic temperature under a Boltzmann distribution. Thus, a further refinement of the fit was attempted by fitting the populations of individual electronic levels. This practice still did not guarantee uniqueness of solutions. For optically thick lines, their intensity will depend upon both upper and lower state density, and whatever variables are responsible for line broadening: typically translational temperature (Doppler) and/or electron density (Stark). The other disadvantage of fitting individual levels is the large number of fit parameters required, many of which may either be covariant with other parameters or insignificant in the fit. Best efforts are made to remove insignificant levels from fitting in the data reported below. The results as presented below are divided by spectral region. No effort is made to perform simultaneous analysis across the different spectral ranges. In many cases, the accuracy of the fit data is going to be determined by the information that is available in the spectrum and how the NEQAIR model is constructed (i.e. epistemic uncertainty). However, the uncertainty reported is the uncertainty in fit parameters (i.e. aleatory uncertainty), and does not include explicitly the uncertainty in the experimental data.

III. Results

A. Vacuum Ultraviolet Spectrum

The most prominent feature in the vacuum ultraviolet is the 174 nm line of atomic nitrogen, which originates from the 3s state of the atom. This line is expected to be optically thick for most of the conditions under study. However, due to the finite resolution of the spectrometer, the overall height or thickness of the line cannot be determined. Therefore, the area under the line is the only meaningful parameter obtained from the measurement. The area under the curve will be dependent upon both the height and width of the line. The height of the line is dependent upon the ratio of excited and lower state density, which would be related to electronic temperature under a Boltzmann distribution. The width of the line depends upon the broadening mechanism involved. If the broadening is assumed to be determined by the Stark effect then the width will be primarily dependent upon electron number density, with weaker dependence upon electron temperature. Figure 3 shows the dependence of the N174

---

* t=translational, r=rotational, v=vibrational, e=electronic, e^-=electron

line intensity upon four of these parameters, where other parameters are held at the equilibrium condition of the 10.74 km/s test condition. All four dependencies are nearly linear on a log-log plot, with a nearly linear sensitivity on electron density, but a square root dependence on N atom (or upper state) density. An inverse square root dependence on ground state density is observed.
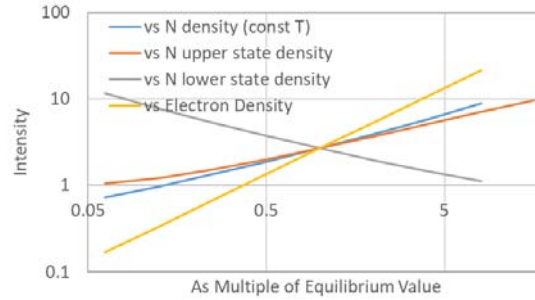
Figure 3. Dependence of N 174 radiance upon different parameters in the flow, relative to equilibrium (10.74 km/s)

The N 174 and N 149 nm lines in the steady region are compared to equilibrium radiance in Figure 4 for the 10.34 km/s condition. While the N 149 nm line is close to predictions, the N 174nm line is significantly higher. The unmatched ratio of these two lines has been observed by other authors [18, 19]. Here, a simultaneous fit of these lines is performed and overlaid on the figure. In order to reproduce the spectrum, the temperature is inferred to be 8800K, which is 700K less than the equilibrium condition of 9573K. Atomic carbon is also added into the fit and found to be present at on the order of 40 ppm. The N atom density is 20% higher than equilibrium value, but the electron density required is over an order of magnitude higher. Even with these deviations, the peak of the N 174 line is not fit, so it appears necessary to use modeling options other than Boltzmann.
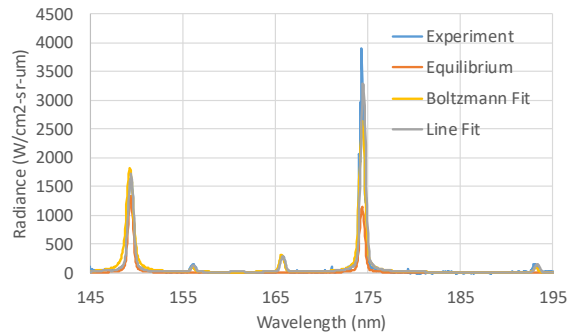
Figure 4. Sample Fit of vacuum ultraviolet spectrum

Table 1. List of Nitrogen atomic lines observed in the near vacuum-ultraviolet region

Wavelength	Upper level			Lower Level			A coefficient
	Energy	Designation	g	Energy	Designation	g	
149.263	86220.51	3s ^{2}P	4	19224.46	2p^3 ^{2}D	6	3.11E+08
149.282	86220.51	3s ^{2}P	2	19233.18	2p^3 ^{2}D	4	3.26E+07
149.468	86137.35	3s ^{2}P	4	19233.18	2p^3 ^{2}D	4	3.46E+08
174.272	86220.51	3s ^{2}P	2	28838.92	2p^3 ^{2}P	2	2.12E+07
174.273	86220.51	3s ^{2}P	4	28839.31	2p^3 ^{2}P	4	1.05E+08
174.525	86137.35	3s ^{2}P	6	28838.92	2p^3 ^{2}P	2	8.35E+07
174.526	86137.35	3s ^{2}P	2	28839.31	2p^3 ^{2}P	4	4.01E+07

The list of atomic lines in this region of the VUV are given in Table 1. There is a triplet at 149 nm and a quartet at 174 nm. From these lines we identify two upper states (3s) and four lower states (2p^3) contributing to the spectrum. These levels are fit simultaneously, yielding the Boltzmann plot in Figure 5. Overlaid on the plot are the concentrations determined at equilibrium, and for best fit Boltzmann and non-Boltzmann cases. The non-Boltzmann

case resembles a Saha equilibrium that passes directly through the three groups of data points. This line requires high ground state densities and low ion densities, so is not physically plausible. Looking at only the three groups of states involved in the fit, the 3s and 2p3 ^{2}P states are consistent with equilibrium, though an overpopulation of the 2p^3 ^{2}D state is required to explain the lower intensity of the 149 nm line. It should be noted that, for optically thick lines, the intensity is more dependent on the ratio of levels than the magnitude of levels. Thus, an underpopulation of the 2p^3 ^{2}P state could also explain the discrepancy. In this case, a Saha distribution may exist that connects the 2p^3 ^{2}P and 3s ^{2}P states to an ion density that exceeds equilibrium, while the 2p^3 ^{2}D state sits in equilibrium with the ground state.
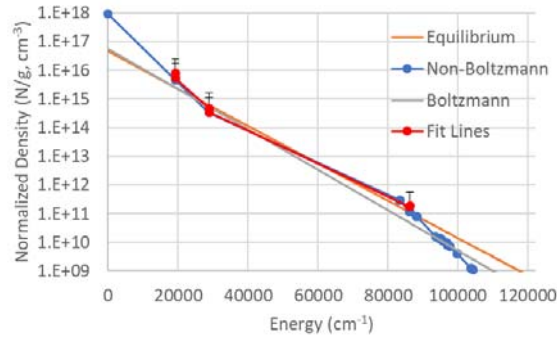

Figure 5. Boltzmann plot obtained from lines in the Vacuum Ultraviolet

B. Ultraviolet Spectrum

The "equilibrium" ultraviolet spectrum is shown in Figure 6, and overlaid with the NEQAIR prediction based upon an incident shock equilibrium condition as calculated by the CEA code [20]. While the general features are present, and in approximately the right intensity, it is apparent that the continuum radiation is underpredicted. The atomic lines observed in this wavelength range are summarized in Table 2. It is apparent from Figure 6 that some atomic lines predicted are not observed, while other lines present are not predicted. The lines that are not observed originate from 3d states of Nitrogen that have energies above the ionization limit. Thus, assuming the A coefficients to be accurate, this would indicate that these states are underpopulated. It is not clear that these states should be included in future radiation calculations or if the lines should be removed from the line list. Some features that are not predicted but are observed include lines from 421-427 nm, which are positively assigned to transitions between the 4p-3s levels of N. These levels are included in the NIST level database but are absent from the NIST line list. These lines have, however, been evaluated in other atomic spectral databases as multiplets. [21] The series of lines involves transitions from 7 upper states to 3 lower states, producing 21 lines (7 triplets) total which are not individually resolved. The two most prominent triplets are given in Table 2. Einstein A coefficients are assigned to these triplets based on their relative magnitude in comparison to the 413-415 nm series, and assuming the relative value within each triplet are the same as for the 415 nm triplet. The impact of including these lines, and removing others, is shown as the modified line list curve in Figure 6. Subsequent analysis is performed with this modified line list.
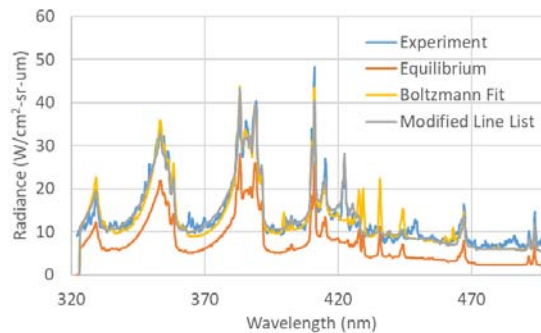

Figure 6. "Equilibrium" spectrum obtained in the ultraviolet, with equilibrium prediction from CEA, and the best-fit Boltzmann spectrum. Also shown is the fit performed with a modified line list.

Table 2. List of Nitrogen atomic lines observed in the ultraviolet region

Wavelength	Upper level			Lower Level			A coefficient
	Energy	Designation	g	Energy	Designation	g	
Observed Lines in NIST/NEQAIR Database							
381.827	112319.8	3p	4	86129.9	3s	2	8.95E+05
382.203	112294	3p	2	86129.9	3s	2	3.70E+06
383.043	112319.8	3p	4	86213.1	3s	4	4.67E+06
383.422	112294	3p	2	86213.1	3s	4	1.89E+06
388.757	111853.1	5p	4	86130.1	3s	2	2.09E+06
389.220	111905.6	5p	6	86213.2	3s	4	2.50E+06
401.114	111060.9	5p	2	86130.3	3s	2	5.75E+05
402.456	111060.9	5p	2	86213.5	3s	4	1.14E+06
409.994	110521	3p	4	86130.4	3s	2	3.48E+06
410.995	110544.9	3p	6	86213.7	3s	4	3.90E+06
411.397	110521	3p	4	86213.6	3s	4	6.62E+05
413.764	107445.6	4p	4	83277.2	3s	2	2.80E+05
414.343	107445.6	4p	4	83311.0	3s	4	6.09E+05
415.148	107445.6	4p	4	83357.8	3s	6	1.01E+06
466.046	107588.5	4p	2	86131.4	3s	2	6.72E+05
466.291	119210	4s	4	97764.2	3p	2	1.51E+06
466.989	107628.3	4p	4	86214.5	3s	4	7.49E+05
467.068	119210	4s	6	97799.8	3p	4	1.80E+06
491.494	106477.8	4p	2	86131.7	3s	2	8.08E+05
493.512	106477.8	4p	2	86214.9	3s	4	1.76E+06
Lines predicted from database but not observed							
427.813	120155.8	3d	4	96781.1	3p	4	5.01E+06
429.321	120150.1	3d	6	96857.5	3p	6	5.21E+06
435.629	119812.9	3d	8	96857.6	3p	6	5.10E+06
443.511	120311.2	3d	2	97763.8	3p	2	2.99E+06
444.245	120309.6	3d	4	97799.5	3p	4	3.81E+06
Lines observed but not in database							
420.999	107037.1	4p	6	83284.1	3s	2	3.77E+05
421.598	107037.1	4p	6	83317.8	3s	4	8.20E+05
422.431	107037.1	4p	6	83364.6	3s	6	1.36E+06
424.007	106868.6	4p	8	83284.1	3s	2	9.96E+04
424.614	106868.6	4p	8	83317.8	3s	4	2.17E+05
425.459	106868.6	4p	8	83364.6	3s	6	3.59E+05

Figure 6 also shows best fits to the spectra obtained by adjusting input parameters for a Boltzmann distribution of states. A similar fit is performed and reported using NEQAIR's non-Boltzmann solver. In both cases, a single temperature is used. The fit parameters obtained are compared to CEA values in Table 3. Errors reported are the error in the fit parameters, and do not represent other sources of uncertainty, such as those created by the construction of the model. For cases where the error exceeds the best fit value, the end of the error range is reported as an upper bound. The best Boltzmann fit to the data is about 300K higher than equilibrium and has about twice the ionization level. The number density of N is fairly close to equilibrium, while the N_2 and N_2^+ densities are about a quarter of and thirty percent higher than equilibrium, respectively. Since these values do not represent a gas in thermodynamic equilibrium, the non-Boltzmann model may be a more appropriate model of the radiation. In this case, the temperature obtained is about 1400K higher than equilibrium and the extracted N_2 and N density are orders of magnitude lower than equilibrium. The N_2 and N_2^+ fits are indeterminant. Electron density (atomic ion) is still almost twice the equilibrium value. In both cases, the CN density required to be consistent with the measurement is on the order of 10^{12} cm^{-3}, which corresponds to about 10^{-5} in mole fraction.

Table 3. CEA predictions for the 10.34 km/s case and comparison of parameters obtained by fitting the spectrum in the ultraviolet.

| Parameter	CEA Equilibrium	Fits				
		Boltzmann	Ratio vs. Eq	Non-Boltzmann	Ratio vs Eq	Independent Levels
T_{rt}	9573 K	9840 ± 120 K	1.03	10900 ± 100 K	1.14	9170 ± 170 K
T_{ve}						10400 ± 300 K
N_2	$5.5 \times 10^{14}\,cm^{-3}$	$<2.8 \times 10^{14}\,cm^{-3}$	0.23	$< 1.1 \times 10^{12}\,cm^{-3}$	10^{-3}	$<1.2 \times 10^{15}\,cm^{-3}$
N	$2.1 \times 10^{17}\,cm^{-3}$	$2.1 \pm 0.4 \times 10^{17}\,cm^{-3}$	0.97	$3.1 \pm 0.1 \times 10^{13}\,cm^{-3}$	10^{-4}	$1.7 \pm 1.1 \times 10^{16}\,cm^{-3}$
N_2^+	$1.0 \times 10^{13}\,cm^{-3}$	$1.3 \pm 0.1 \times 10^{13}\,cm^{-3}$	1.3	$<1.2 \times 10^{14}\,cm^{-3}$	1.0	$6.5 \pm 1.0 \times 10^{14}\,cm^{-3}$
N^+ (e^-)	$6.6 \times 10^{15}\,cm^{-3}$	$1.3 \pm 0.1 \times 10^{16}\,cm^{-3}$	1.9	$1.2 \pm 0.1 \times 10^{16}\,cm^{-3}$	1.8	$1.1 \pm 0.03 \times 10^{16}\,cm^{-3}$
CN	N/A	$2.3 \pm 0.1 \times 10^{12}\,cm^{-3}$	--	$2.0 \pm 0.1 \times 10^{12}\,cm^{-3}$	--	$<3.0 \times 10^{13}\,cm^{-3}$

The deviation in number densities from equilibrium may be attributed to a number of factors. First, the fit is based upon an assumed Einstein coefficient for each transition, which has some uncertainty associated with it. Thus, any error in this coefficient will propagate through to the densities derived. Second, the fits are based upon electronically excited states of the atoms and molecules, and the total number density is thus inferred based upon either a Boltzmann relationship, or the solution to the non-Boltzmann equations, both of which are highly dependent upon the temperature. Small errors in temperature may produce significantly larger errors in number density. Thus, further fits are performed allowing the densities of individual states as fit parameters. The most sensitive levels included in the fit are detailed in Table 4.

Table 4. Levels fit independently in the ultraviolet

| Species	Level	Energy (cm^{-1})	Contribution
N_2	C $^3\Pi_u$	89,137	2nd Positive (337, 358, 380 nm)
N	4p ^{2}S	106477.8	491,493 nm
	4p ^{4}P	107037.1	421-422 nm
	4p ^{4}S	107445.6	413-415 nm
	4p ^{2}P	107588.5	466 nm
	4p ^{2}P	107628.3	467 nm
	3p ^{2}D	110521	410, 411 nm
	3p ^{2}D	110544.9	411 nm
	5p ^{2}S	111060.9	401,402 nm
	5p ^{2}D	111853.1	389 nm
	5p ^{2}D	111905.6	389 nm
	3p ^{2}P	112294	382, 383 nm
	3p ^{2}P	112319.8	381, 383 nm
	4s ^{2}D	119210	466 nm
N_2^+	B $^2\Sigma_u^+$	25461	1st Negative (331, 358, 391, 428 nm)

From these fits, the final column of Table 3 shows the translational-rotational temperature to be 400K below equilibrium and the vibrational-electron to be 500K above equilibrium. Note that the electronic temperature here can only influence states that are not included in the level fit, so this temperature is primarily an indication of vibrational temperature. Additionally, the ground state density for several of the species is no longer determined by the fit as only features from electronically excited states are present. Of these, the electron density still is significant as it determines the magnitude of the bound-free radiation and is 60% higher than equilibrium. The Boltzmann plot for this fit is shown in Figure 7, along with the state densities determined from the equilibrium, Boltzmann, and non-Boltzmann fits. A few of the levels lie near to the equilibrium line, while others are near to the non-Boltzmann best fit. The non-Boltzmann fit produces a near-Boltzmann distribution, with higher temperature and lower number density than either the Boltzmann or equilibrium solution. This non-Boltzmann line goes through the scatter of the individually fit state densities, as expected for a line of best fit. The Saha normalized ion number density corresponding to the independent line fit is marked with "*" on the graph and is nearly identical to that obtained in the non-Boltzmann fit. Comparing the distribution obtained to this value suggests that some states (4p ^{4}P/^{4}S/^{2}P, 3p ^{2}D, 5p ^{2}S/^{2}D, 4s ^{2}D) are closer to a Saha distribution, while others (4p ^{2}S, 5p ^{2}D, 3p ^{2}P) may follow a Boltzmann

distribution. This suggests some modification to the non-Boltzmann grouping in NEQAIR may be warranted. In particular, currently all 4p states are grouped together, as are 5p.
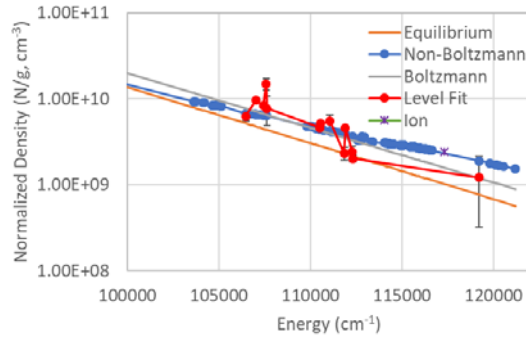
Figure 7. Boltzmann plot of the N atom states responsible for UV emission

The fits with these lines were performed next over the spatially resolved length of the image. From these fits are extracted trends in temperature and number densities of excited states. The temperature is shown in Figure 8(a). The shock position, as determined by pressure sensors, coincides with the point where the translational temperature has fully relaxed, rather than at its peak value, as would be expected. The reason for this is not clear; it may be indicative of a lag in response time between shock arrival and the pressure sensors used for time of arrival. The initially high translational/rotational temperature of 35,000K relaxes to about 9300K over a distance of 0.7 cm. The vibrational temperature rises and overshoots this value, up to about 13,000K, before relaxing back to similar values. This overshoot of vibrational temperature to translational temperature has been predicted in previous CFD models but has not been previously noted in experimental data to our knowledge. On the scale of Fig. 1, the temperature seems fairly constant after about 1 cm, though the fluctuations are as large as 1000K and is probably more indicative of the accuracy of the spectra and their subsequent fits than it is indicative of thermal non-equilibrium. The N^+ ion density, which is approximately equal to the electron number density, is shown in Figure 8(b) and is inferred from fits of the bound-free continuum. The N^+ concentration rises to near equilibrium levels within a cm, near the point at which the vibrational and rotational temperatures have relaxed to the same value. The ion density then rises steadily behind the shock front. This behavior has been previously observed and tentatively attributed to deceleration of the shock [22, 23].


(a)   (b)
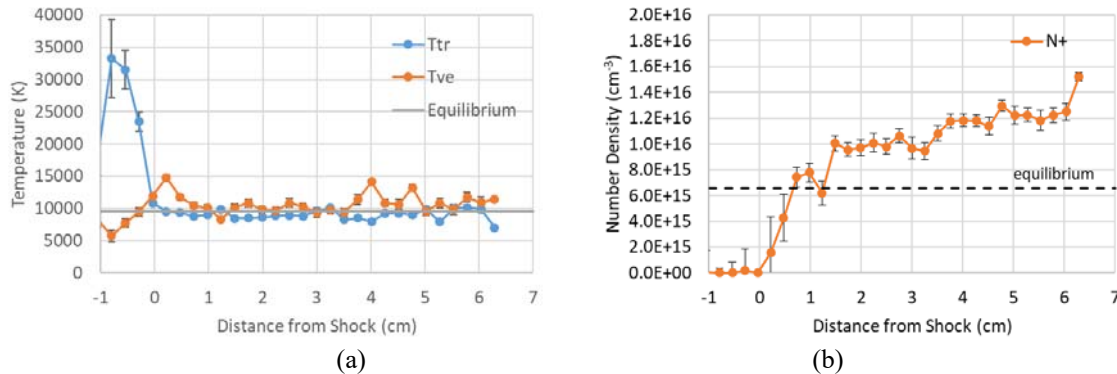
Figure 8. Fits to emission data versus position at 10.34 km/s.

Fits of excited molecular states of N_2, N_2^+ and CN are shown in Figure 9(a), where these states should be directly responsible for the molecular emission observed. To derive ground state densities from these trends requires some intervening assumption about the nature of the state population. The densities of N_2 and N_2^+ are derived from these data applying three assumptions, as shown in Figure 9(b) and (c). Using a single temperature Boltzmann distribution, the N_2^+ density peaks at about 6×10^{13} cm^{-3} and drops quickly to a steady value of 1.3×10^{13} cm^{-3}, where it remains. If a two-temperature fit is allowed, the N_2^+ peak is less, at around 3×10^{13} cm^{-3}, and falls over the same time span to a steady value of 8×10^{12} cm^{-3}. For a single temperature fit, the N_2 density is first estimated at 9 $\times 10^{15}$ cm^{-3} near the shock front location, then drops to near the detection limit within 2 cm. In comparison, the frozen N_2 density would be 1.2×10^{17} cm^{-3}. If the fit is allowed to accommodate multiple temperatures, the N_2

density is inferred at less than 10^{15} cm^{-3} at most points. It is noted that, when allowing for a two-temperature fit, the vibrational and translational fit temperatures do not converge to the same value, but may differ by as much as 2000-3000K. The inferred number densities are not greatly influenced by whether the molecules are assumed to be determined by Boltzmann or non-Boltzmann state populations.
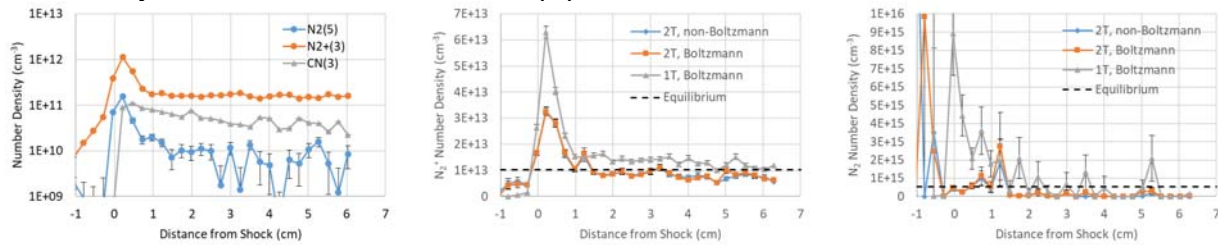
Figure 9. (a) Fits of the excited levels of N_2, N_2^+ and CN as a function of distance behind the shock. (b,c) Inferred densities of N_2^+ and N_2, respectively, from the excited state data using different models of state populations.

The trend of atomic excited states, grouped as discussed above is shown in Figure 10. Increased spatial averaging is required to reduce the noise to reasonable levels. The 4p states are observed right at the shock front and do not vary much more than the noise level through the shock. The 4p ^{2}S level, which is lower in energy than the other 4p states, rises more gradually than the other 4p states. The next two groups also show a slower rise through the shock front and are continuing to rise after 6 cm. Fits of the 4s ^{2}D density is statistically insignificant early in the shock, but is detected above the fitting error after about 2 cm. The ion density, normalized by the Saha factor, is co-plotted with the data. It is seen to closely follow the 4s ^{2}D density, as it rises later in the shock. This suggests the 4s ^{2}D concentration to be in Saha equilibrium. The corresponding Boltzmann distribution is shown at 4 positional locations, -0.3 cm, +0.2 cm, +1.0 cm and +6.0 cm. The rising of the entire N atom distribution is observed between these first two points. The 4s 2D level deviates from Boltzmann behavior at these positions. The slope is seen to be increasing, indicating a rising electronic temperature, up to the 1 cm point. The Saha normalized ion density is shown as a point of the same color but not connected to the line plot. At 1 and 6 cm, it is close to the line connecting the excited states, however at earlier points, it is too low to be observed on the axis scale. The Boltzmann curves suggest that a Boltzmann or Saha distribution may be a good assumption for the majority of the measurement time.
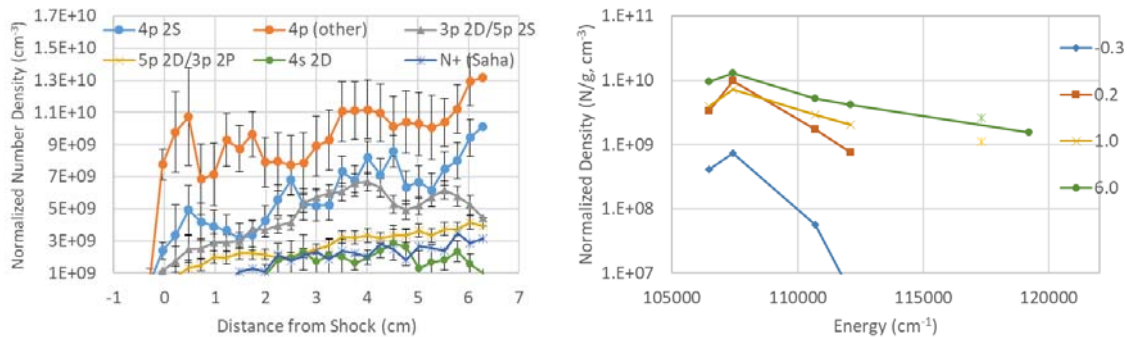
Figure 10. The progression of levels responsible for atomic lines in the ultraviolet. (left) as normalized level density versus time, (right) as Boltzmann plot at locations of -0.3, 0.2, 1.0 and 6.0 cm

C. Visible/Near Infrared Region

Spectra obtained in the visible in the steady region of the shock are shown in Figure 11(a) along with the prediction obtained based on equilibrium composition and the best fit of the spectra. An underprediction of continuum radiation is again apparent in the spectrum. The atomic line features observed are given in Table 5. There are 46 lines from the NIST database that are identified with confidence and given in the table. Due to blending with stronger lines or continuum, there are at least 16 additional lines that are likely present but not identified with confidence. The presence of Hydrogen impurity is confirmed by identification of the Balmer-α line at 656 nm. There are additional lines observed that are not identified in the NIST atomic spectral database, but can

be confirmed through other sources. These lines are given in Table 5, with A coefficients taken from Ref. [21]. The relative intensities of the 517 nm multiplet are estimated. Figure 11(b) shows a zoom in to the 500-650 nm region of the spectrum, where the impact of adding these lines is apparent. It is also apparent from the figure that there are still additional lines missing from the spectrum.
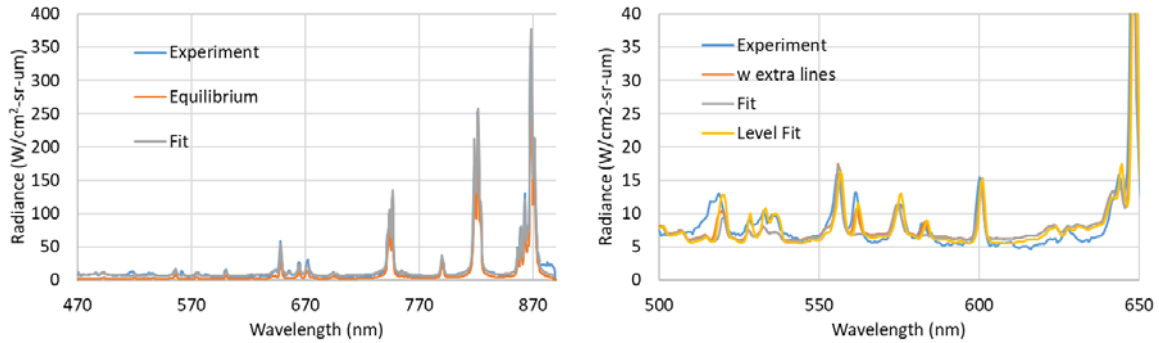

Figure 11. Spectrum in the visible portion of the spectrum, (right) zoom into the 500-640 nm region.

Table 5. List of Nitrogen atomic lines observed in the visible region

Wavelength	Upper level			Lower Level			A coefficient
	Energy	Designation	g	Energy	Designation	g	
Observed Lines in NIST/NEQAIR Database							
519.984	112807.6	5d ^{2}P	2	93581.5	3p ^{2}S	2	1.87E+06
520.161	112801	5d ^{2}P	4	93581.5	3p ^{2}S	2	1.87E+06
528.12	107037.1	4p ^{4}P	6	88107.3	2p^4 ^{4}P	6	2.45E+05
532.862	106868.6	4p ^{4}D	8	88107.3	2p^4 ^{4}P	6	2.05E+05
535.662	106814.5	4p ^{4}D	6	88151.2	2p^4 ^{4}P	4	1.41E+05
536.701	106778.3	4p ^{4}D	4	88151.2	2p^4 ^{4}P	4	1.07E+05
537.261	106778.3	4p ^{4}D	4	88170.6	2p^4 ^{4}P	2	8.34E+04
556.034	112861.4	5d ^{4}F	10	94881.8	3p ^{4}D	8	1.42E+06
573.995	112910.6	5d ^{4}D	6	95493.7	3p ^{4}P	4	7.49E+05
575.25	112911.1	5d ^{4}D	8	95532.1	3p ^{4}P	6	1.06E+06
600.847	110220.1	4d ^{2}P	4	93581.5	3p ^{2}S	2	3.58E+06
642.064	110401.4	4d ^{4}D	6	94830.9	3p ^{4}D	6	8.97E+05
644.094	110403.2	4d ^{4}D	8	94881.8	3p ^{4}D	8	1.33E+06
648.27	110303.2	4d ^{4}F	10	94881.8	3p ^{4}D	8	4.90E+06
648.375	110212.4	4d ^{4}F	6	94793.5	3p ^{4}D	4	3.67E+06
648.481	110247.3	4d ^{4}F	8	94830.9	3p ^{4}D	6	4.20E+06
664.496	109926.7	5s ^{4}P	6	94881.8	3p ^{4}D	8	3.49E+06
670.611	110401.4	4d ^{4}D	6	95493.7	3p ^{4}P	4	2.51E+06
672.261	110403.2	4d ^{4}D	8	95532.1	3p ^{4}P	6	3.56E+06
676.961	110300	4d ^{4}P	6	95532.1	3p ^{4}P	6	8.02E+05
692.667	109926.7	5s ^{4}P	6	95493.7	3p ^{4}P	4	7.75E+05
694.518	109926.7	5s ^{4}P	6	95532.1	3p ^{4}P	6	1.83E+06
695.16	109856.5	5s ^{4}P	4	95475.3	3p ^{4}P	2	1.03E+06
697.919	109856.5	5s ^{4}P	4	95532.1	3p ^{4}P	6	9.83E+05
698.203	109812.2	5s ^{4}P	2	95493.7	3p ^{4}P	4	2.04E+06
731.898	110447	4d ^{2}D	4	96787.7	3p ^{2}D	4	5.41E+05
737.851	110300	4d ^{4}P	6	96750.8	3p ^{4}S	4	1.30E+06
742.364	96750.8	3p ^{4}S	4	83284.1	3s ^{4}P	2	5.64E+06
744.23	96750.8	3p ^{4}S	4	83317.8	3s ^{4}P	4	1.19E+07
746.831	96750.8	3p ^{4}S	4	83364.6	3s ^{4}P	6	1.96E+07
754.621	110035.7	5s ^{2}P	2	96787.7	3p ^{2}D	4	2.85E+06
755.091	110103.8	5s ^{2}P	4	96864	3p ^{2}D	6	1.79E+06
758.757	109926.7	5s ^{4}P	6	96750.8	3p ^{4}S	4	7.01E+05

762.818	109856.5	5s ⁴P	4	96750.8	3p ⁴S	4	6.90E+05
789.898	112319.8	3p ²P	4	99663.4	3s ²D	6	2.82E+07
791.542	112294	3p ²P	2	99663.9	3s ²D	4	3.13E+07
818.486	95532.1	3p ⁴P	6	83317.8	3s ⁴P	4	8.21E+06
818.801	95493.7	3p ⁴P	4	83284.1	3s ⁴P	2	1.25E+07
821.634	95532.1	3p ⁴P	6	83364.6	3s ⁴P	6	2.26E+07
824.239	95493.7	3p ⁴P	4	83364.6	3s ⁴P	6	1.31E+07
856.774	97805.8	3p ²P	4	86137.4	3s ²P	2	4.86E+06
859.4	97770.2	3p ²P	2	86137.4	3s ²P	2	2.09E+07
862.924	97805.8	3p ²P	4	86220.5	3s ²P	4	2.67E+07
868.028	94881.8	3p ⁴D	8	83364.6	3s ⁴P	6	2.53E+07
868.34	94830.9	3p ⁴D	6	83317.8	3s ⁴P	4	1.88E+07
871.17	94793.5	3p ⁴D	4	83317.8	3s ⁴P	4	1.29E+07
Lines observed but not in database							
517.109	107445.6	4p ⁴S	4	88107.3	2p⁴ ⁴P	6	1.00E+04
518.285	107445.6	4p ⁴S	4	88151.2	2p⁴ ⁴P	4	6.00E+05
518.807	107445.6	4p ⁴S	4	88170.6	2p⁴ ⁴P	2	5.00E+05
561.810	112681.4	6s ⁴S	6	94881.8	3p ⁴D	8	2.03E+06
583.114	112681.4	6s ⁴S	6	95532.1	3p ⁴P	6	1.12E+06

Table 6 shows the parameters obtained from the fit spectrum shown in Figure 11 using different population options in NEQAIR. When fits are performed using a Boltzmann distribution, the temperature obtained is within 80K of equilibrium. The N atom and ion density are 70% and 20% larger than equilibrium, respectively, while the N_2 and N_2^+ densities are 45 and 13 times larger. The density of hydrogen inferred indicates a mole fraction on the order of 10^{-3}. Performing the fit with the non-Boltzmann solution changes these numbers somewhat, though the difference is within the fit uncertainty. It is interesting to compare these parameters to those obtained using only the ultraviolet data. The values for temperature and ion density are much closer to equilibrium, although the molecular species are now substantially larger. A fit of the spectrum was also performed allowing the density of individual states, as specified in Table 7, to be fit parameters. As the excited states of molecules were fit parameters, the ground state and total density could no longer be determined by the fit, though the upper bound is much more consistent with equilibrium values than those obtained assuming the molecules to be in a Boltzmann distribution. The ion density extracted is fairly consistent with equilibrium, while the N atom density is several times larger. Several levels with identified lines (Table 5) were removed from the fit because they were fit with large uncertainties due to overlapping lines. The population of these levels would then depend upon the vibrational-electronic temperature and thus influence that value. The state distribution obtained by this fit is shown as a Boltzmann plot in Figure 12. For comparison, the equilibrium solution, and Boltzmann/non-Boltzmann fit solutions are also shown. The non-Boltzmann fit produces a nearly identical distribution to the Boltzmann solution, which is a consequence of the electron density being close to equilibrium. The higher N atom number density causes the distribution to be larger than the equilibrium line. The levels fit are mostly consistent with the non-Boltzmann solution with the exception of the four levels corresponding to the 4p states of N. These levels correspond to the underpredicted multiplet from 528-537 nm in Figure 11(b). The disagreement is more likely due to an inaccuracy in the Einstein coefficient, or possibly a contribution from additional unidentified lines, rather than indicative of an overpopulation of these states.
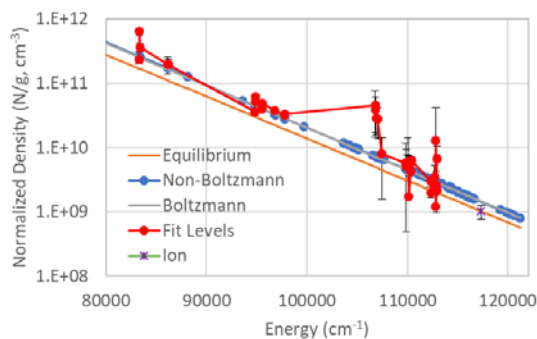

Figure 12. Boltzmann plot obtained from the fit of lines in the visible

Table 6. CEA predictions for the 10.34 km/s case and comparison of parameters obtained by fitting the spectrum in the visible.

Parameter	CEA Equilibrium	Fits				
		Boltzmann	Ratio vs. Eq	Non-Boltzmann	Ratio vs Eq	Independent Levels
T_{rt}	9573 K	9490 ± 90 K	0.99	9640 ± 170 K	1.01	9790 ± 2490 K
T_{ve}						9200 ± 130 K
N_2	$5.5 \times 10^{14}\,cm^{-3}$	$2.5 \pm 0.5 \times 10^{16}\,cm^{-3}$	45	$2.1 \pm 0.5 \times 10^{16}\,cm^{-3}$	37	$<1.0 \times 10^{15}\,cm^{-3}$
N	$2.1 \times 10^{17}\,cm^{-3}$	$3.6 \pm 0.5 \times 10^{17}\,cm^{-3}$	1.7	$4.3 \pm 0.6 \times 10^{17}\,cm^{-3}$	2.0	$7.3 \pm 1.7 \times 10^{17}\,cm^{-3}$
N_2^+	$1.0 \times 10^{13}\,cm^{-3}$	$1.3 \pm 0.1 \times 10^{14}\,cm^{-3}$	13	$1.2 \pm 0.1 \times 10^{14}\,cm^{-3}$	12	$<8.7 \times 10^{13}\,cm^{-3}$
N^+ (e^-)	$6.6 \times 10^{15}\,cm^{-3}$	$8.0 \pm 0.7 \times 10^{15}\,cm^{-3}$	1.2	$7.8 \pm 0.2 \times 10^{15}\,cm^{-3}$	1.2	$6.6 \pm 1.6 \times 10^{15}\,cm^{-3}$
H	N/A	$3.6 \pm 2.1 \times 10^{14}\,cm^{-3}$	--	$3.5 \pm 1.8 \times 10^{14}\,cm^{-3}$	--	$7.6 \pm 3.3 \times 10^{14}\,cm^{-3}$

Table 7. Levels fit independently in the visible

Species	Level	Energy (cm^{-1})	Contribution
N_2	B $^3\Pi_g$	59,619	1st Positive (500-700 nm)
N	3s ^4P	83284.1	742.4, 818.8 nm (lower state)
	3s ^4P	83317.8	744.2, 818.5, 868.3, 871.2 nm (lower state)
	3s ^4P	83364.6	746.8, 821.6, 824.2, 868.0 nm (lower state)
	3s ^2P	86137.4	856.8, 859.4 nm (lower state)
	3s ^2P	86220.5	862.9 nm (lower state)
	3p ^4D	94793.5	871.2 nm
	3p ^4D	94830.9	868.3 nm
	3p ^4D	94881.8	868.0 nm
	3p ^4P	95493.7	818.8, 824.2 nm
	3p ^4P	95532.1	818.5, 821.6 nm
	3p ^4S	96750.8	742.4, 744.2, 746.8 nm
	3p ^2P	97770.2	859.4 nm
	3p ^2P	97805.8	856.8, 862.9 nm
	4p ^4D	106778.3	536.7, 537.3 nm
	4p ^4D	106814.5	535.7 nm
	4p ^4D	106868.6	532.9 nm
	4p ^4P	107037.1	528.1 nm
	4p ^4S	107445.6	517-519 nm
	5s ^4P	109812.2	698.2 nm
	5s ^4P	109856.5	695.2, 697.9, 762.8 nm
	5s ^4P	109926.7	664.5, 692.7, 694.5, 758.8 nm
	5s ^2P	110035.7	754.6 nm
	5s ^2P	110103.8	755.1 nm
	4d ^4F	110303.2	648.3 nm
	4d ^2P	110220.1	600.8 nm
	4d ^4D	110403.2	644.1, 672.3 nm
	3p ^2P	112294	791.5 nm
	3p ^2P	112319.8	789.9 nm
	6s ^4P	112681.4	561.8, 583.1 nm
	5d ^2P	112801	520.2 nm
	5d ^2P	112807.6	520.0 nm
	5d ^4F	112861.4	556.0 nm
	5d ^4D	112910.6	574.0 nm
	5d ^4D	112911.1	575.3 nm
N_2^+	B $^2\Sigma_u^+$	25461	1st Negative (320-390 nm)

The fits are next performed as a function of position from the shock front. Due to the lack of strong molecular features in many of the visible spectra, the translational-rotational temperature was indeterminate for much of the fit and a single temperature fit was employed instead. The fits are performed in three ways: assuming a Boltzmann distribution of states, a non-Boltzmann distribution, and fitting state populations. The temperature trend is shown in Figure 13(a). When the level fit is performed, the temperature increases steadily with distance behind the shock front, from roughly 8,000 to 10,000K. A decrease in temperature is inferred at about 5 cm behind the shock front, which is coincident with contact front arrival. For the Boltzmann fit, the trend in temperature is less severe, increasing from about 9,000 to 9,800K. The non-Boltzmann fit is more similar to the Boltzmann fit but is more variable. The species number densities are covariant to the temperature in the fits. Fits retrieving low temperatures also yield unrealistically large N atom and/or N_2 densities, and thus this data is not presented for the level fit. The N_2 number density plot is in Figure 13(b), and shows, after an initial decrease, the N_2 density fluctuating around 2×10^{16} cm^{-3}. The electron density (Figure 13(c)) shows a steady increase over 3cm, plateaus, then begins to decrease. Using Boltzmann versus non-Boltzmann fits for both electron and N_2 number density has some effect on the values, but does not alter the trend. The trend of the N_2 (B) and N_2^+ (C) states from the level fit are shown in Figure 14. A sharp peak is observed at the shock front, and thereafter the data is relatively constant. Figure 15(a) shows the trend in individual atomic levels. The levels have been grouped with like states, where both the energy and number density trends are relatively similar. These grouped levels are also shown in the Boltzmann plot of Figure 15(b) for 4 different spatial locations. The 3s levels all display nearly constant density while they are detected, but the higher energy levels are increasing over the first cm, with the higher energy 3p and 5s levels taking slightly longer to reach their steady concentration. The Boltzmann plot shows the slope of the line increasing steadily, consistent with a rising electron temperature. The curve nearly matches the equilibrium condition (light blue line) at 0.2 cm, and increases beyond equilibrium at 1 and 5 cm. The Saha normalized ion density from the non-Boltzmann fit is also shown on the Boltzmann plot and approximately follows the trend of the level density lines.
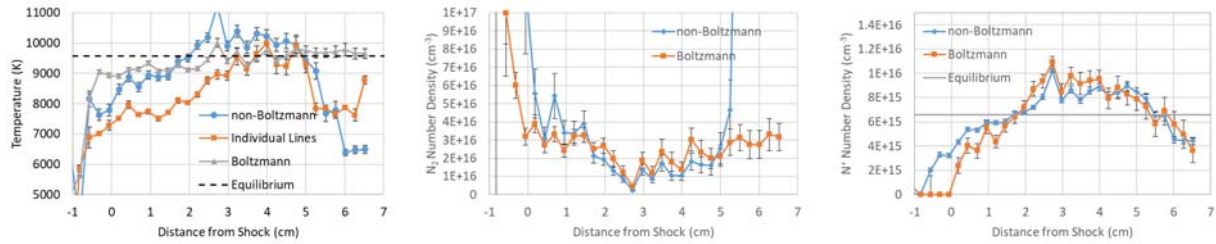

Figure 13. Temperature and number density fits obtained from the visible part of the spectrum
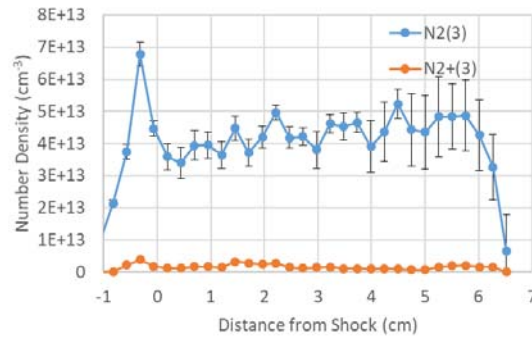

Figure 14. Densities of excited molecular states as a function of position.
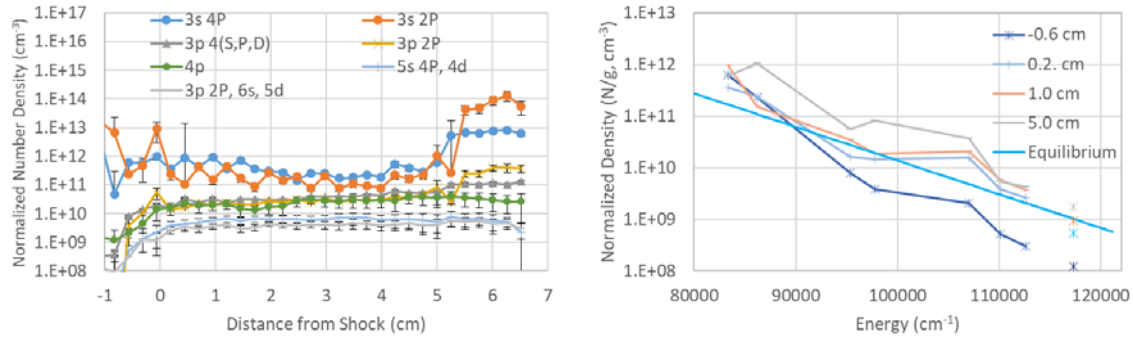
Figure 15. Fit of atomic levels vs. position (left) and as Boltzmann plot at different points (right)

D. Ionization

Ionization levels were reported in Ref. [9] in the form of electron density measurements determined by Stark broadening of the hydrogen Balmer-α line. The data was derived from a different shock than the one discussed above, but at similar velocity conditions. In this section, we evaluate the impact of different rate models on the ionization and compare it to the experimental measurement. The measured electron density was determined by fitting spectra whose radiance has been spatially averaged due to finite resolution of the measurement system and motion of the shock during the exposure time. To examine how this resolution impacts the extracted electron density, the simulation is subjected to the same resolution limits and analysis method as is applied to the experimental data. An artificial 3D spectrum is produced using the predicted electron density profile. This result is then convolved with spatial and instrument resolution functions [9] in both directions to give the synthetic spectrum. This spectrum is next fit with Lorentzian functions to extract an equivalent electron density, in the same way that the experimental electron density was derived.

The rates involved in N_2 shocks are the following:

$$N_2 + M \leftrightarrow N + N + M \tag{1}$$
$$N_2 + e^- \leftrightarrow N + N + e^- \tag{2}$$
$$N + e^- \leftrightarrow N^+ + e^- + e^- \tag{3}$$
$$N + N \leftrightarrow N_2^+ + e^- \tag{4}$$
$$N^+ + N_2 \leftrightarrow N_2^+ + N \tag{5}$$

Rates for these five processes were originally compiled by Park in 1990 [24], then revised in 1993 [25]. Alternative rates for the electron impact dissociation of N_2 (Reaction (2)) were determined theoretically by Bourdon and Vervich [26] and adopted by Johnston [27] for hypersonic air modeling. This rate was 4-5 orders of magnitude lower than the rate employed by Park, which was adjusted to match experimental measurements in an expanding nitrogen flow. The current authors re-evaluated this rate using NIST recommended electron impact dissociation rate cross-sections [28] and determined a rate that lies between the rates of Bourdon and Park [4]. These rates are shown in Figure 16(a).

The current authors have also re-evaluated the rate of reaction (5), which was an order of magnitude estimate by Park, by integrating experimentally measured collision cross-section measurements [29]. This new rate is shown in Figure 16(b) and is several orders of magnitude lower than that employed by Park. The impact of this rate on ionization is discussed below. The fact that some of these relatively simple rates remain unknown and have such significant impact on flow properties even for such a simple reaction system underlines the need for further study of this nature.
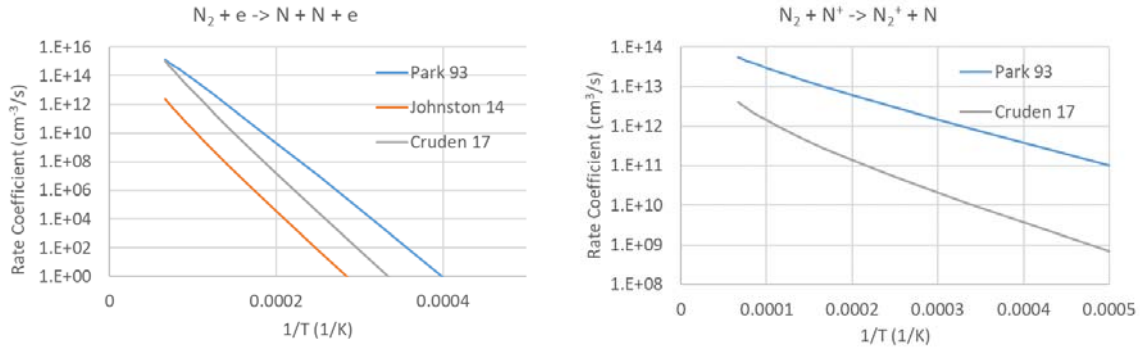
Figure 16. Reaction rates proposed for electron impact dissociation of N_2 and charge exchange in N_2.

The impact of these rates on ionization are shown in Figure 17. The model labeled as Johnston [27] is the Park [25] model with the dissociation rate (Reaction (2)) replaced by that of Bourdon [26]. The model labeled as Cruden substitutes rates from [4] for Reactions (2) and (5). All three models predict some overshoot of equilibrium in the electron number density although the ionization rate employed is the same. The overlaid temperature trends help elucidate the cause of the overshoot. In general, the ionization peak lags the thermal non-equilibrium region. In the Park model, the high rate of Reaction (2) causes a faster temperature relaxation (due to endothermicity) and a larger concentration of N atom available to initiate ionization through Reaction (4). This in turn accelerates Reaction (2). By the time the electron density reaches an equilibrium level, the temperature is nearly fully relaxed and thus the overshoot is small. The Johnston and Cruden models give virtually the same temperature trends, owing to the slower rate of Reaction (2), which otherwise helps to promote thermal equilibration. This higher temperature drives the ionization process and thus the electron density overshoots until the temperature drops to the equilibrium temperature. The Cruden model shows a greater overshoot in electron density due to the slower charge exchange process. As the temperature drops, three body recombination is slow and thus the recombination of electrons proceeds through first converting N^+ to N_2^+ via Reaction (5) and then dissociatively recombining to N atoms through Reaction (4). The lower ion exchange rate causes this recombination process to be slower and hence electron density returns to equilibrium much more slowly than the other two models.
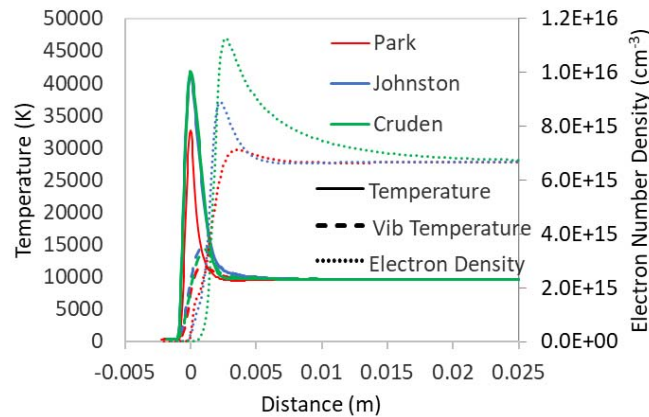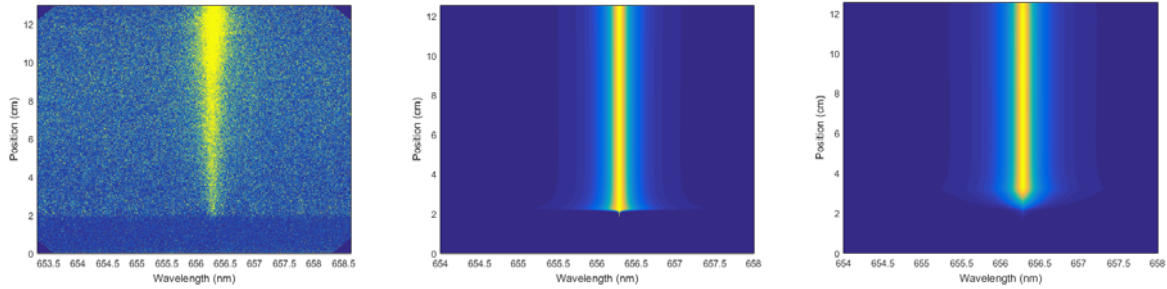

Figure 17. Predicted ionization and temperature trends at 10.34 km/s with three different chemistry models.

Figure 18. Plot of Hydrogen line shape/intensity as a function of wavelength and position. (a) experimental measurement, (b) predicted, (c) predicted with spatial resolution functions applied.

The 3D spectra derived from these three profiles, accounting for instrument resolution affects, are shown in Figure 18. The electron densities extracted from these spectra are shown in Figure 19, overlaid with the experimental data. The effect of the instrument resolution is apparent in the blunting of the overshoot for all three reaction models. In the case of the Park model, this obscures the initial overshoot and creates a transient that is roughly consistent with the observed data which does not indicate an overshoot. At the shock front, the experimental data displays a detection limit near 10^{15} cm^{-3}. The modeled spectra, however, are unable to reproduce the experimental limit and are instead truncated at electron densities from 2-4 × 10^{15} cm^{-3}. Attempts to fit the simulated spectra in this early region of the shock result in a reversal of the electron density trend because the stronger radiance "mixes" with the weakly radiating region due to application of the spatial resolution function.
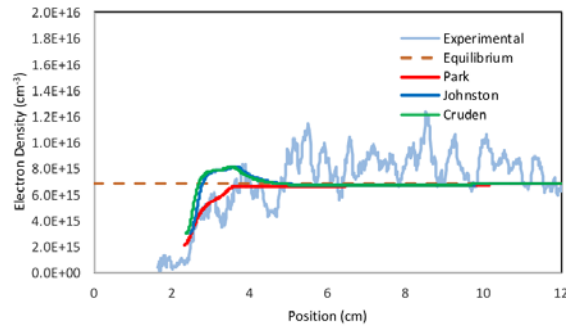
Figure 19. Experimentally derived electron densities, and model predicted electron densities after adjusting for spatial resolution functions.

IV. Conclusion

An analysis of shock tube data collected in pure Nitrogen at 10.3 km/s (nominal) is presented. In particular, the analysis has used the NEQAIR program to extract the spatial concentration and temperature of excited states from EAST radiation data. In order to perform the analysis, the underlying NEQAIR model is presumed to be correct, allowing data to be extracted that can be compared to expected values. Fits in the ultraviolet put the N atom density and temperature within 3% of equilibrium, if a Boltzmann distribution of states is assumed to apply. In the visible range, the fit temperature is within 1% of equilibrium for either Boltzmann or non-Boltzmann distributions, though the N density is large by a factor of 2. In the ultraviolet, comparison to equilibrium shows an underprediction of continuum radiation, which is linked to the ionization fraction and electron number density. The inferred electron density would be approximately twice equilibrium to explain the data. Analysis of the continuum magnitude versus position shows the electron density to be near to equilibrium at the shock front, and increasing above equilibrium further from the shock. Similar behavior has been observed in air shocks based upon Stark broadening measurements [23]. In the visible range, the increasing in intensity is realized as a steadily increasing temperature in the fits. Whatever the underlying cause, this type of behavior has been observed in previous works and attributed to deceleration of the shock as it travels down the tube [22].

Detailed examination of the atomic line contributors in the ultraviolet and visible range has been conducted, and many of the more prominent lines identified and enumerated in this work. Some lines originating from 3d states above the ionization limit are not observed at predicted intensities. Other lines are found to be missing from the NIST line list, particularly those originating from 4p and 6s states of the N atom. These lines are relatively strong in

some other line lists, allowing their identification as important features. Besides these lines, there are additional features that remain unpredicted in the spectrum. There are a great number of excited states of N, many of which are not catalogued by NIST, that lie in the energy range appropriate for producing features here, making identification difficult without having a good estimate of their line strengths. It is conceivable that some of these states might blend together in a way that explains part of the continuum underlying the spectrum.

Finally, the electron densities reported in Ref [9] are analyzed in terms of rate models, accounting for finite temporal and spatial resolution. The important rates that change between these models are the rate of charge exchange between N^+ and N_2, and electron impact dissociation of N_2, and its inverse. Three different rate models are used to simulate the Stark broadening, and extract the electron density profile in the same way the experiment does. This process blunts the predicted equilibrium overshoot of electron density. However, models based upon the electron impact dissociation cross-section are still observed to predict an overshoot which is not observed experimentally. The Park model, on the other hand, shows a very good agreement with the data.

Acknowledgements

References

1. Brandis, A. M., Johnston, C. O., Cruden, B. A., Prabhu, D., and Bose, D., "Uncertainty Analysis and Validation of Radiation Measurements for Earth Reentry," *Journal of Thermophysics and Heat Transfer,* Vol. 29, No. 2, 2015, pp. 209-221.
2. Brandis, A. M., Johnston, C. O., and Cruden , B. A., "Investigation of Non-equilibrium Radiation for Earth Entry," AIAA Paper 2016-3690.
3. Cruden, B. A., Brandis, A. M., and Johnston, C. O., "Development of a Radiative Heating Margin Policy for Lunar Return Missions," *Journal of Thermophysics and Heat Transfer,* Vol. 32, No. 2, 2018, pp. 303-315.
4. Cruden, B. A., and Brandis, A. M., "Measurement and Prediction of Radiative Non-equilibrium for Air Shocks Between 7-9 km/s," AIAA Paper 2017-4535.
5. Grover, M. S., Singh, N., Schwartzentruber, T. E., and Jaffe, R. L., "Dissociation and internal excitation of molecular nitrogen due to N2-N collisions using direct molecular simulation," AIAA Paper 2017-0660.
6. Jaffe, R. L., Grover, M., Venturi, S., Schwenke, D. W., Valentini, P., Schwartzentruber, T. E., and Panesi, M., "Comparison of Potential Energy Surface and Computed Rate Coefficients for N2 Dissociation," *Journal of Thermophysics and Heat Transfer,* Vol. 32, No. 4, 2018, pp. 869-881.
7. Macdonald, R. L., Grover, M. S., Schwartzentruber, T. E., and Panesi, M., "State-to-State and Direct Molecular Simulation Study of energy transfer and dissociation in nitrogen mixtures," AIAA Paper 2018-0239.
8. Chaudhry, R. S., and Candler, G. V., "Statistical Analyses of Quasiclassical Trajectory Data for Air Dissociation," AIAA Paper 2019-0789.
9. Brandis, A. M., and Cruden , B. A., "Shock Tube Radiation Measurements in Nitrogen," AIAA Paper 2018-3437.
10. Johnston, C. O., and Brandis, A. M., "Modeling of nonequilibrium CO Fourth-Positive and CN Violet emission in CO2–N2 gases," *Journal of Quantitative Spectroscopy and Radiative Transfer,* Vol. 149, 2014, pp. 303-317.
11. Cruden, B. A., Brandis, A. M., and MacDonald, M. E., "Characterization of CO Thermochemistry in Incident Shockwaves," AIAA Paper 2018-3768.
12. Brandis, A. M., Johnston, C. O., Cruden, B. A., Prabhu, D. K., Wray, A. A., Liu, Y., Schwenke, D. W., and Bose, D., "Validation of CO 4th positive radiation for Mars entry," *Journal of Quantitative Spectroscopy and Radiative Transfer,* Vol. 121, 2013, pp. 91-104.
13. Brandis, A. M., Johnston, C. O., Cruden, B. A., and Prabhu, D. K., "Investigation of Nonequilibrium Radiation for Mars Entry," AIAA Paper 2013-1055.
14. Cruden, B. A., Martinez, R., Grinstead, J. H., and Olejniczak, J., "Simultaneous Vacuum Ultraviolet through Near IR Absolute Radiation Measurement with Spatiotemporal Resolution in an Electric Arc Shock Tube," AIAA Paper 2009-4240.
15. Cruden , B. A., and Brandis, A. M., "Updates to the NEQAIR Radiation Solver," *Radiation in High Temperature Gases*. St. Andrews, UK, 2014.
16. Whiting, E., Park, C., Liu, Y., Arnold, J., and Paterson, J., "NEQAIR96, Nonequilibrium and Equilibrium Radiative Transport and Spectra Program: User's Manual," NASA RP-1389, 1996.
17. http://www.nist.gov/pml/data/asd.cfm, 2019.
18. Lemal, A., Nishimura, S., Nomura, S., Takayanagi, H., Matsuyama, S., and Fujita, K., "Analysis of VUV radiation measurements from high temperature air mixtures," AIAA Paper 2016-0740.
19. Takayanagi, H., Fujita, K., Ishida, H., Yamada, K., and Abe, T., "Radiation intensity measurement in VUV wavelength region behind strong shock wave for future sample return missions," AIAA Paper 2014-2965.

20. McBride, B. J., and Gordon, S., "Computer program for calculation of complex chemical equilibrium compositions and applications II. User's Manual and Program Description," NASA RP-1311-P2, June 1996.
21. Liu, Y., Huo, W., Wray, A., and Carbon, D., "Electron Stark Broadening Database for Atomic N, O, and C Lines," AIAA Paper 2012-2739.
22. Brandis, A. M., Cruden, B. A., Prabhu, D., Bose, D., McGilvray, M., and Morgan, R. G., "Analysis of Air Radiation Measurements Obtained in the EAST and X2 Shocktube Facilities," AIAA Paper 2010-4510.
23. Cruden, B. A., "Electron Density Measurement in Reentry Shocks for Lunar Return," *Journal of Thermophysics and Heat Transfer,* Vol. 26, No. 2, 2012, pp. 222-230.
24. Park, C., *Nonequilibrium Hypersonic Aerothermodynamics*, New York: John Wiley & Sons, 1990.
25. Park, C., "Review of chemical-kinetic problems of future NASA missions. I - Earth entries," *Journal of Thermophysics and Heat Transfer,* Vol. 7, No. 3, 1993, pp. 385-398.
26. Bourdon, A., and Vervisch, P., "Study of a low-pressure nitrogen plasma boundary layer over a metallic plate," *Physics of Plasmas (1994-present),* Vol. 4, No. 11, 1997, pp. 4144-4157.
27. Johnston, C. O., "Study of Aerothermodynamic Modeling Issues Relevant to High-Speed Sample Return Vehicles," VKI 2013-AVT-218.
28. Itikawa, Y., "Cross sections for electron collisions with nitrogen molecules," *Journal of Physical and Chemical Reference Data,* Vol. 35, No. 1, 2006, pp. 31-53.
29. Phelps, A. V., "Cross Sections and Swarm Coefficients for Nitrogen Ions and Neutrals in N2 and Argon Ions and Neutrals in Ar for Energies from 0.1 eV to 10 keV," *J. Phys. Chem. Ref. Data,* Vol. 20, No. 3, 1990, pp. 557-573.